Grain boundary-mediated plasticity in aluminum films unraveled by a statistical approach combining nano-DIC and ACOM-TEM

Paul Baral, Ankush Kashiwar, Michaël Coulombier, Laurent Delannay, Khalid Hoummada, Jean-Pierre Raskin, Hosni Idrissi, Thomas Pardoen

Grain boundary mediated plasticity in aluminum films unraveled by a statistical approach combining nano-DIC and ACOM-TEM

Paul BARAL [1,2,†], Ankush KASHIWAR [1,3,†], Michaël COULOMBIER [1], Laurent DELANNAY [1], Khalid Hoummada [4], Jean Pierre RASKIN [5], Hosni IDRISSI [1,3], Thomas PARDOEN [1,6]*

(1) Institute of Mechanics, Materials and Civil Engineering (IMMC), UCLouvain, B-1348, Louvain-la-Neuve, Belgium

(2) Univ. Lyon, Mines Saint Etienne, CNRS UMR 5307 LGF, Centre SMS, 42100 Saint Etienne, France

(3) EMAT, University of Antwerp, Groenenborgerlaan 171, B-2020, Antwerp, Belgium

(4) IM2NP, Aix Marseille Univ/CNRS, UMR 7334, 13397 Marseille, France

(5) Institute of Information and Communication Technologies, Electronics and Applied Mathematics (ICTEAM), UCLouvain, B-1348, Louvain-la-Neuve, Belgium

(6) WEL Research Institute, avenue Pasteur 6, B-1300, Wavre, Belgium

* Corresponding author: thomas.pardoen@uclouvain.be

[†]Paul Baral and Ankush Kashiwar should be considered as co-first authors. Both authors have equally contributed to the work.

ABSTRACT

Nanomechanical on-chip testing is combined with nanoscale *in situ* digital image correlation and automated crystal orientation mapping in TEM to deliver novel statistically representative quantitative data about the deformation mechanisms in nanocrystalline aluminum films. The films are very ductile, with a rare stable multiple necking process with local strains reaching up to 0.45 and macroscopic elongation up to 0.17. The strain fields with resolution below 100 nm are related to the underlying microstructure and crystallographic orientation maps. This reveals nanoscopic shear bands forming preferentially along GB with high misorientations, tilted at +/- 45° with respect to loading direction. The analysis of these data prove that the strong strain delocalization process is promoted by GB migration and grain rotation, leading to large strain rate sensitivity. The distribution of misorientation angles between grains evolve during deformation. The GB with misorientation between 20 and 40 °, which are the GBs with highest energy, involve the largest strains.

1. Introduction

Nanocrystalline (nc) and ultrafine-grained (UFG) metals exhibit outstanding mechanical strength and fatigue resistance compared to their coarse-grained (cg) counterparts. Thin films made of nc or UFG metals are potential candidates for hard and tough coatings, for structural components in MEMS/NEMS, and conductive layers in microelectronic devices [1–4]. However, the use of such films is often restricted by the limited ductility due to low dislocation storage capacity within small-sized grains [5,6]. In such systems, some strain hardening capacity can be induced by nanotwins or secondary phases restoring then moderate to high resistance to plastic localization [7–9]. Ductility can also sometimes be significantly improved by raising the rate sensitivity, owing for instance to a complex interplay between thermally activated dislocation-based processes and grain boundary (GB) mechanisms [10,11]. This has driven a strong research interest in unraveling the fundamentals and magnitude of the competing deformation mechanisms in these materials at the smallest length scales [12–22]. Among others, the dislocation-based deformation processes nc and UFG metals include intragranular dislocation-glide within the grains [19–21] as well as at the GBs [21,23,24]. The interaction of dislocations with GBs including their absorption or re-emission from the GBs is enhanced due to a large fraction of GBs [20,25–27]. The dislocation-mediated plasticity in nc metals is often characterized by global texture evolution [28,29] due to the rotation of individual grains and their interaction with neighbors as revealed by kernel average misorientation (KAM) [30] and intragranular misorientation (mis2mean) [12,31] local analysis.

One aspect that is often lacking in the current literature to assess scenarios for these competing deformation mechanisms is the need for quantitative data with sufficient statistical value particularly with respect to the deformation fields connected to the microstructure characteristics. Microscopic strain fields can nowadays be acquired by digital image correlation (DIC) in a SEM for sample sizes in the range of the millimeter down to several tens of micrometers with spatial resolution between 50 and 500 nm This results from the continuous improvement of surface patterning methods [32–34]. Such strain fields are linked to the microstructure by coupling DIC and *in situ* electron back scatter diffraction (EBSD) during deformation [35–40]. Linne *et al.* quantitatively estimated both grain boundary sliding and slip transmission in micro-scale aluminum samples with a typical grain size of a few tens of microns and DIC spatial resolution of 410 nm [38,41]. Vermeij *et al.* [37,40] as well as Yavuzyegit *et al.* [42] produced strain maps with a spatial resolution down to some tens of nanometers. They paved the way to probe intra-granular plasticity and grain boundary-mediated plasticity at very small scales. Nevertheless, such HR-EBSD analysis cannot be applied to nanocrystalline materials nor freestanding films due to insufficient spatial resolution and film thickness under backscatter diffracting conditions.

The deformation of thin films has been widely studied with in situ TEM nanomechanical testing [14,21,24,43,44]. Using in situ TEM straining and dark-field TEM (DFTEM) imaging, Shan *et al.* showed grain rotation in nc-Ni thin film (mean grain size 10 nm) being accommodated by diffusive processes in GB regions [45]. However, DFTEM imaging offers visualization of only a limited number of grains that are under suitable diffraction conditions. Wang *et al.* demonstrated by high-resolution TEM (HRTEM) on nc-Pt that the grain rotation involved dislocation climb at GB and the evolution of misorientation angle was studied by considering the change of Frank-Bilby dislocation content in the GB [46]. Li *et al.* employed *in situ* TEM straining with bright field TEM (BFTEM) imaging to show the operation of GB sliding and migration for specific GBs in nc-Au films [47]. BFTEM has been proven highly advantageous for detailed analysis of intra- and inter-granular plasticity during in situ deformation [20,21,47,48]. However, deformation-induced grain rotations are the cause of sudden changes in the diffraction contrast, which are difficult to reliably interpret. Moreover, local characterization within a sampling size of only a few tens of nm is seldom fully representative of the deformation mechanism. Kobler *et al.* performed automated crystal orientation mapping in the TEM (ACOM-TEM) during in situ straining of nc-Pd [12]. This allowed a high spatial resolution (1 nm) with statistically significant information related to the distributions of grain size, crystal orientation, GB misorientation and intragranular lattice curvature. Mompiou *et al.* used this approach together with complementary BFTEM imaging to quantify grain growth and grain rotation in sub-micron Al thin films deformed to 7% strain [49]. Elastic strain field measurements at spatial resolution from 0.5 to 4 nm

were performed with a field of view of 20 to 200 nm [50–52]. Yet, strain distributions over larger samplings would be required to explain the microstructure evolution in nc or UFG materials. A key challenge is the correlation between high-resolution measurements of the local strain and high-resolution microstructural characterization over a wide sampling area inside a TEM.

In the present study, a novel approach is demonstrated combining nanomechanical lab-on-chip (LOC) testing with both nanoscale *in situ* digital image correlation (nano-DIC) and automated crystal orientation mapping in TEM (ACOM-TEM). Nano-DIC is capable of high-resolution quantification of both the in-plane shear strains and the grain rotations. The spatial distribution of strains at the GBs as well as within the grains is captured over the whole deformed polycrystal. Strain and rotation maps are correlated with the microstructural characteristics including GB character, GB misorientation as well as crystal orientation and extended defects, which can be explored by ACOM-TEM. Owing to these new capabilities and rich data, it has been possible to unravel the elementary plasticity mechanisms leading to the large ductility of the tested UFG aluminum freestanding films. Plastic deformation in UFG aluminum films as well as in other nanocrystalline FCC material has been extensively studied [10,14,21,23,24,43,44,53–56] but the interpretation of the data remains debated due to the variety of deposition processes and microstructures. The combination of LOC testing, nano-DIC and ACOM-TEM opens the possibility of making a closer link between the local strains and microstructure of polycrystalline materials at nanoscales with a statistically significant sampling size. This offers new insights into the complex interplay between intra-granular and GB plasticity in nanocrystalline materials.

2. Material and methods

2.1. Film deposition and on-chip test method

The principle of the tensile-on-chip test method (TOC) developed at UCLouvain [57] is illustrated in Fig. 1. The design and fabrication of these experiments based on photolithography are reported with more details in refs [57,58]. Only the salient features of the method are given here. Once the deposited structure is freed from the substrate (by chemical etching), the partial release of residual stress causes the actuators to pull on the test material. The resulting overall stress and strain are deduced from the change of length of the beams.

The actuator material is a silicon nitride Si_3N_4 produced by low-pressure chemical vapor deposition (LPCVD). The Young's modulus, measured by nanoindentation, is equal to 250 GPa, and the residual stress is close to 1 GPa in tension. The layer thickness is measured by ellipsometry after deposition and

is equal to 125 nm. The actuator layer is patterned to generate actuator beams with different lengths – i.e. the longer the beam the larger the tensile strain applied to the specimen.

The specimen layer is deposited by sputtering from a 99.999 % pure aluminum target at room temperature and 1.2 mTorr pressure under a current of 300 mA in Ar gas. The film has been characterized by atom probe tomography and only Al atoms were found (see supplementary material Fig. S1). The grains grow with a columnar shape across the film thickness, which has been observed by cutting a cross-section of a specimen by focus ion beam (FIB) (see Fig. S2.d in the supplementary material). The columnar structure is evidenced with GBs nearly perpendicular to the silicon substrate, which has been reported by Pletea *et al.* [59].

The sample thickness, measured with a profilometer Dektak150, is equal to 240 nm. Sputtering involves a shadow effect, which reduces the deposition rate at the edges of the specimen – i.e. close to the photo-resin walls. The resulting cross-section has rounded edges with a thickness lower than the center of the cross-section. The ratio between the real cross-section area and the ideal rectangular shape is taken into account when determining the engineering stress. Photolithography and lift-off are used to pattern the film with a dogbone shape (see Fig. 1.a). The length and width of the specimens are varied between 10 - 800 µm and 1 - 10 µm, respectively. Here, only specimens with length of 25 µm and width of 2.5 µm are investigated, see supplementary material, Table 1.

After deposition and patterning, electron beam evaporation from indium pellets with a 99.90 % purity is performed (see Fig. 1.b and supplementary material Fig. S2). The speckles cover only the test specimen [37,60]. The deposition rate is set to 1 $Å.s^{-1}$ with a targeted thickness of 5 nm, leading to equiaxed indium particles of 8.1 nm average size with a small scatter of ±2 nm considering the 25^{th} and 75^{th} percentile. The particle size distribution is provided in supplementary material (Fig. S3) and is very close to the one characterized by Klavzer *et al.* [34].

Finally, the structures are released from the silicon substrate by selective dry etching (see Fig. 1.c) using XeF_2 gas by iteration of pulses until the silicon under the specimen and actuator is completely removed. The actuator contracts and pulls on the specimen. The displacement of reference cursors is measured under force equilibrium conditions several minutes after the loading has been applied (see Fig. 1.d and e). This provides an estimate of the specimen elongation, which will be referred to as macro-strain in contrast with the local strain deduced from DIC. The cursor displacement also corresponds to the shortening of the actuating beam, out of which the stress is deduced by assuming a linear elastic behavior of the Si_3N_4 actuator.

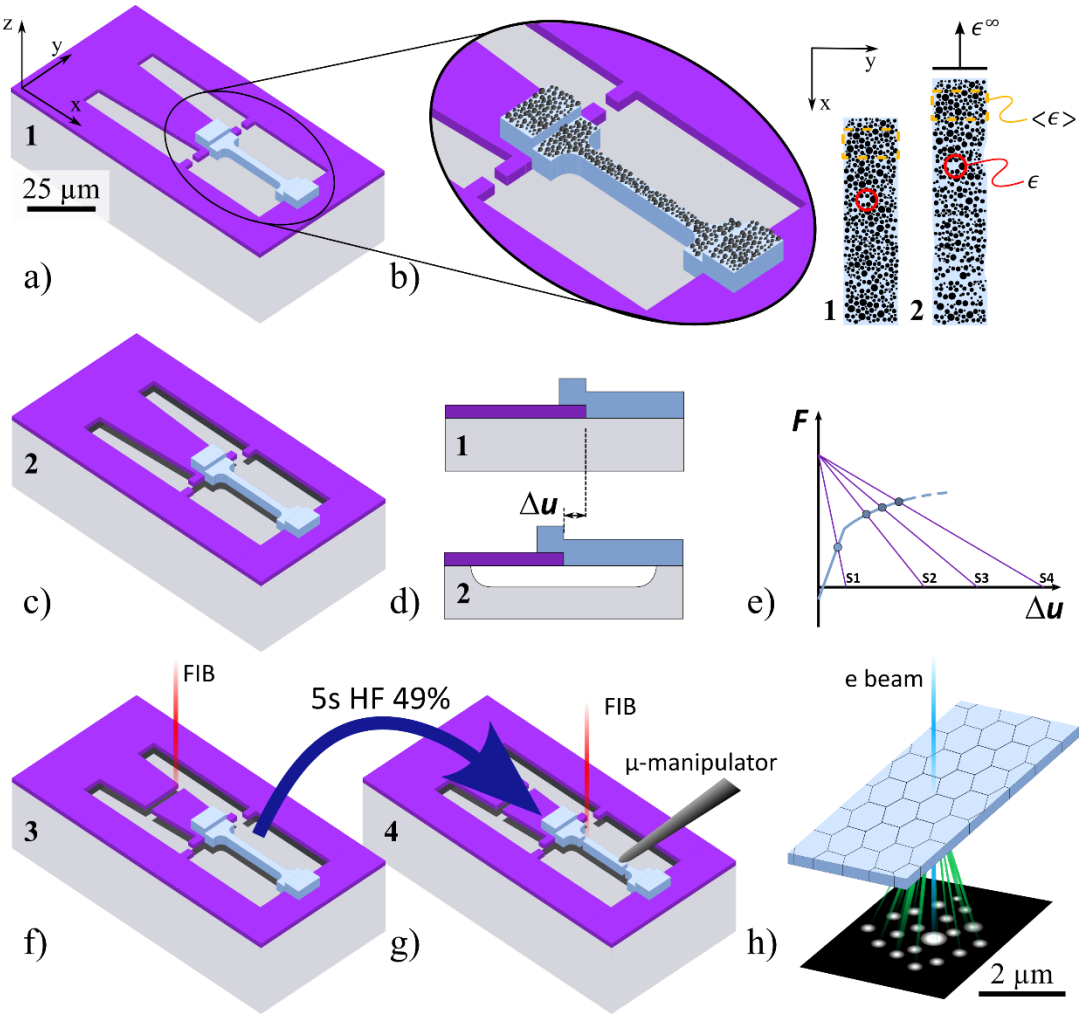

Figure 1 Schematic of the on-chip fabrication process, measurement and characterization: a) patterning of the actuator and specimen, b) zoom on the specimen after deposition of indium nano-particles and representation of the DIC principle, c) release of the test structure, d) measurement of the cursors displacement after release and equilibrium of the test structure, e) representation of the force against displacement of each test structure and equilibrium points dictated by the specimen mechanical behavior, f) unloading of the specimen to be observed in TEM by FIB cutting, g) manipulation the specimen after removing the indium nano-particles with HF and h) characterization of the specimen by ACOM-TEM.

2.2. Nano-digital image correlation

The strain field on the top surface of the Al beams is determined by DIC, using a speckle of indium nano-particles for image correlation. These indium particles adhere to the specimen and are disconnected from each other. Therefore, they do not significantly affect the specimen loading, nor the deformation mechanisms under investigation.

One image with a resolution of 2048 x 1536 pixels is taken for each TOC structure both before and after release. All images are acquired at a working distance of 5 mm and magnifications of 10k and

20k. The pixel resolution is 11 and 5.5 nm, respectively. The scanning electron microscope (SEM) image acquisition is performed by integrating 5 fast image scans in order to minimize the image distortion due to drift. The resulting images can be slightly blurred.

Displacement maps are generated using the Matlab script Ncorr developed by Blaber *et al.* [61], which is well suited to handle high local strains. The algorithm treats the best-correlated subsets before the worst ones, which reduces error propagation. Hence, the highly deformed regions are treated at the end of the DIC analysis. The components of the strain tensor are computed from the displacement map inside subsets with a radius of 15 pixels. The spatial shift between two adjacent subsets is 1 pixel. The three in-plane components of the Lagrangian strain tensor are computed from the local gradient of the displacement field as

$$\epsilon_{xx} = \frac{1}{2}\left(\left(\frac{du}{dx}\right)^2 + \left(\frac{dv}{dx}\right)^2 + 2\frac{du}{dx}\right), \quad (1)$$

$$\epsilon_{yy} = \frac{1}{2}\left(\left(\frac{du}{dy}\right)^2 + \left(\frac{dv}{dy}\right)^2 + 2\frac{dv}{dy}\right), \quad (2)$$

$$\epsilon_{xy} = \frac{1}{2}\left(\frac{du}{dy} + \frac{dv}{dx} + \frac{du}{dx}\frac{du}{dy} + \frac{dv}{dx}\frac{dv}{dy}\right), \quad (3)$$

with u and v being the displacements along the $\vec{x}$ and $\vec{y}$ directions, respectively. If incompressibility is assumed (thus neglecting elastic strains) and unmeasurable out-of-plane shear disregarded [37], the equivalent von Mises strain ϵ_{VM} is estimated as:

$$\epsilon_{VM} = \frac{2}{\sqrt{3}}\left(\epsilon_{xx}^2 + \epsilon_{yy}^2 + \epsilon_{xy}^2 + \epsilon_{xx}\epsilon_{yy}\right). \quad (4)$$

The rotational component of the transformation is reflected by the skew-symmetric part of the in-plane displacement gradient:

$$\omega_{xy} = \frac{1}{2}\left(\frac{du}{dy} - \frac{dv}{dx}\right). \quad (5)$$

2.3. TEM characterization

The microstructure is characterized by TEM on both the undeformed specimen and the specimen deformed to 0.165 macrostrain. In order to facilitate the TEM characterization of the deformed specimen, the In particles are removed by dipping into liquid HF 49% for 5 s, see schematics of Fig. 1.f-

g. As the removal of the native oxide on the Al specimen is likely to induce softening, the actuators of the selected test structures are cut with a focus ion beam (FIB) [62] before dipping the structures in HF (see Fig. 1.f). This prevents any further deformation. HF wet etching is followed by rinsing in 3-isopropanol solution baths and critical point drying to prevent stiction on the underlying substrate. The cut-off specimen is transferred to an Omniprobe TEM lift-out grid with the aid of a micromanipulator inside a Helios Nanolab 600i focused ion beam (FIB) (see Fig. 1.g).

Bright-field TEM (BFTEM) and darkfield TEM (DFTEM) imaging is carried out on a ThermoFisher Osiris F20 TEM to characterize dislocations and grain boundaries (GBs). Automated crystal orientation mapping in TEM (ACOM-TEM) is performed on a ThermoFisher Tecnai G2 equipped with the NanoMEGAS ASTAR system which is used for quantitative analysis of the polycrystalline microstructure (see Fig. 1.h). ACOM-TEM involves an electron beam precessing at 0.5°, a camera length of 44 mm and a step size of 5 nm. The ACOM-TEM maps are processed using the MTEX-5.2.beta2 toolbox to analyze the grain size distribution, crystallographic texture, kernel average misorientation (KAM) as well as character of the GBs. For grain identification, a segmentation angle of 2° is used whereas the KAM analysis is performed for up to 5th order neighbors with maximum threshold angle of 2°, to obtain maps with reduced noise.

3. Results

3.1. Overall mechanical response and local strain distribution

The tensile response of the Al film is shown in Fig. 2.a. The red line corresponds to a Young's modulus of 70 GPa, as expected for Al. Each dot corresponds to one TOC test structure with a different length ratio of the two beams (actuator and sample). Only a few of them involve a small strain, as we focus here on the plastic strain regime. A large ductility is found as the longitudinal strain (averaged over the sample length) reaches a tensile elongation of 0.17.

The mean hardening exponent $n = 0.14$ is calculated from the variation of the stress with the plastic strain (see supplementary material Fig. S5). Creep/relaxation measurements, using the same on-chip technique [63], provide the strain rate sensitivity exponent m = 0.05±0.02, assuming that the yield stress is linked to the strain rate according to a simple power law $\sigma = K\,\dot{\epsilon}^m$. The average rate sensitivity exponent is determined based on the progressive relaxation of the stress in nine specimens deformed between 0.012 and 0.043 macro-strain (see supplementary material Section 6). This conforms with a previous study by Gianola *et al.* [64] on pure Al films ($m \approx 0.04$ for 150 nm thickness and $m \approx 0.08$ for 300 nm thickness). The large standard deviation in our measurement may be due to

the inhomogeneous microstructural changes occurring during relaxation – i.e. grain growth and other competing mechanisms – [63–65], as described in section 3.2.

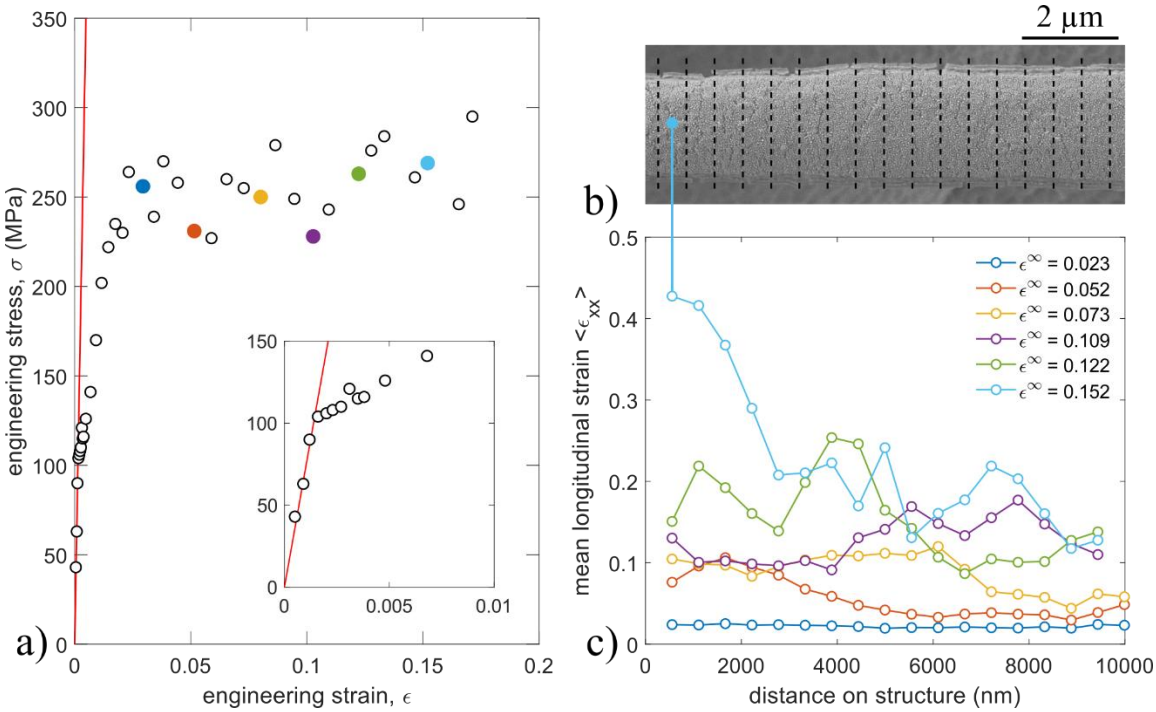

Figure 2 Uniaxial tension response of 240 nm thick Al thin films: a) engineering stress versus engineering strain of freestanding Al thin film, b) top view of a specimen after 0.14 macro-strain and c) evolution of the local longitudinal strain along the length of different specimen undergoing macroscopic strains ranging from 0.023 up to 0.15.

Fig. 2.b shows that soon after the elasto-plastic transition ($\epsilon_{VM} > 0.025$), the longitudinal strain measured by nano-DIC analysis ceases to be uniform along specimen length. Multiple onsets of necking are found, evidenced by local maxima in the distribution of the longitudinal strain shown in Fig. 2.c. The formation of necks may also explain the slight scattering of the results in Fig. 2.a above 0.025 macro-strain. Indeed, the engineering stress appearing in Fig. 2.a is an average value assuming a constant cross-section area, which does not exactly conform to SEM observations.

Figure 3 shows the microscopic distribution of the equivalent von Mises strain (Eq. 4), as deduced from the DIC measurements on three different specimens deformed at, respectively, 0.023, 0.038 and 0.059 macro-strain. As highlighted by the arrows in Fig. 3, the deformation tends to localize along wavy bands. These will be shown to correspond to GB locations in Section 3.2. Microscopic plastic localization already shows up in the specimen with 0.023 macro-strain and is amplified at larger macro-strains. Referring to Fig. 2, the onset of the microscopic localization of deformation in GB regions occurs right after the elastic-plastic transition, when the macroscopic longitudinal strain ceases to be uniform.

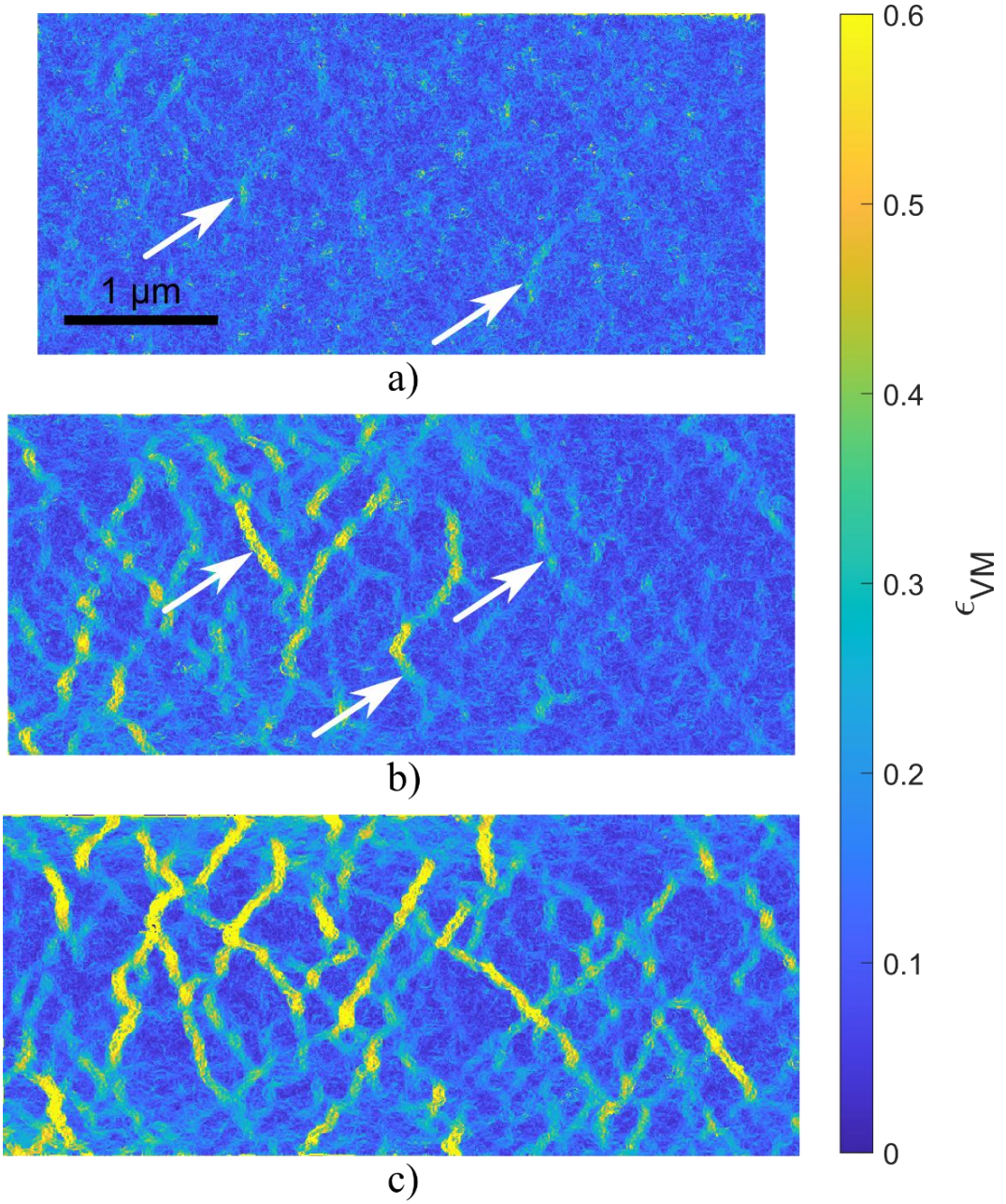

Figure 3 von Mises strain maps inside the Al specimens deformed at a macro-strain equal to a) 0.023 (TOC 04), b) 0.038 (TOC 08), and c) 0.059 (TOC 14).

In order to highlight the presence of rigid body rotation of some regions – e.g. grains or groups of grains, named clusters –, we investigate the rotation field (Eq. 5) associated to low strain regions. Fig. 4.a represents the equivalent strain ϵ_{VM} in a region of a specimen deformed at a macro-strain of 0.122 (TOC 32). In Fig. 4.b, the positive and negative values of ϵ_{xy} inside the plastic localization bands tilted, respectively, at + and – 45° relative to the tensile axis confirm that they contribute to the elongation of the beam. The moderately deformed regions ($\epsilon_{VM} < 0.18$) are individualized as clusters and the rotation field ω_{xy} in each of them is represented in Fig. 4.c. Clusters are assumed to undergo uniform rotation if the average ω_{xy} value is larger than 1.5 times its standard deviation. Fig. 4.d represents

clusters satisfying this condition. Fig. 4.e is a schematic of the rigid body rotations of the microstructure elements deduced from Fig. 4.b and 4.d. It indicates the shear lines (blue for negative and red for positive) and the corresponding rotation of clusters. Fig. 4.d and 4.e show both identical and opposite rotations of adjacent clusters – e.g. couples 2/3, 5/7, 6/8 and couple 1/2, respectively. Finally, Fig. 4.f represents the statistics stemming from the entire specimen surface (see Fig. S7 in supplementary material) of the clusters undergoing almost uniform rotation (see Fig. 4.d). The magnitude of the average rotation is plotted as a function of the cluster radius. The red line highlights the upper trend of the data. Smaller clusters are more prone to large rotation during plastic deformation.

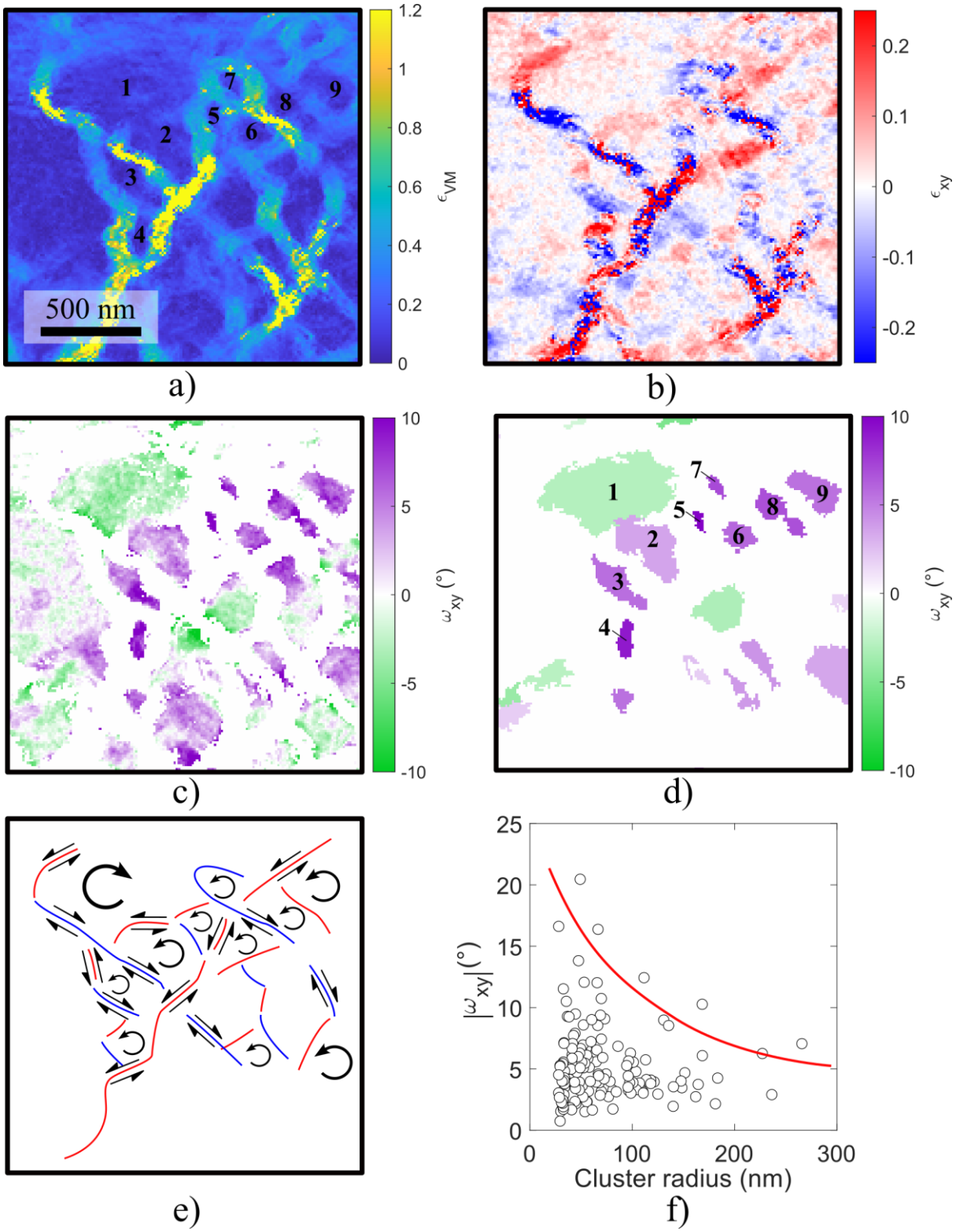

Figure 4 Strain and rotation maps determined based on nano-DIC after a macro-elongation of 0.122: a) Equivalent von Mises strain map exhibiting curly-shaped highly deformed region; b) shear strain ϵ_{xy}; c) rigid body rotation ω_{xy} calculated from nano-DIC, without taking into account the most highly deformed regions (ϵ_{VM} < 0.18); d) homogeneous rotation of clusters for which the average rotation is significantly larger than its standard deviation; e) schematic of the clusters rigid body rotation together with the shear components along the clusters boundaries; f) absolute rotation magnitude as a function of the cluster equivalent radius calculated over the entire specimen (from a map larger than the one presented in this figure).

3.2. Microstructure characterization

Fig. 5 shows the evolution of microstructure during the TOC experiment. Both the virtual BF-STEM image and the crystal orientation map are obtained from ACOM-TEM with a spatial resolution of 5 nm. The first specimen is in the undeformed state (Fig. 5(a-b)) whereas the elongation of the second specimen is equal to 0.165 (Fig. 5 (c-d)). Both the diffraction contrast and the orientation indexing indicate that the equiaxed grain morphology is preserved during the deformation. Moreover, for the deformed specimen, the through-thickness microstructure is characterized by computed the correlation coefficient map as well as by imaging the crystals orientations from the front and back of the specimen. This analysis is presented in supplementary material, Fig. S4. It highlights the fact that the grains are mainly columnar structures that run through the film thickness.

ACOM-TEM also provides the statistical distributions of grain sizes and GB misorientations. The GB characteristics, respectively, before and after deformation are compared by considering both the orientation of the GB plane relative to the tensile axis and the lattice misorientation across the GB. The curvilinear structure detector algorithm of Steger [66] is used to compute the tilt angle of the normal of every GB segment, relative to the tensile axis. The GB misorientation is determined from ACOM-TEM. The grain boundary orientation is discretized by steps of 22.5° from 0 to 90° and the same is done for misorientation with discretization steps of 10° from 0 to 70°. A matrix of 28 orientations and misorientations is created with 4x7 couples. Fig. 6.a and 6.b show the probability distribution inside this matrix for, respectively, the undeformed specimen and the deformed one. Fig. 6.a indicates a high fraction of misorientation angles around 45°. Fig. 6.b shows that the proportion of such high-angle GBs significantly decreases after deformation. Fig. 6.c gathers complementary information about misorientation evolution after deformation. It represents the integral of the distribution for any given misorientation angle. Finally, Fig. 6.d shows the grain size distributions of the undeformed and deformed specimens. The mean grain sizes in the undeformed and deformed specimens are equal to 84 nm and 120 nm, respectively. This suggests deformation-driven grain growth. The fact that the specimen edges are thinner, as a result of the deposition process (see Section 2.1), probably explains why the largest grains in Fig. 5.c and 5.d are mostly located away from the sample edges. A quantitative study of the grain size distribution along the width of the specimen is available in supplementary material (Fig. S8 and S9).

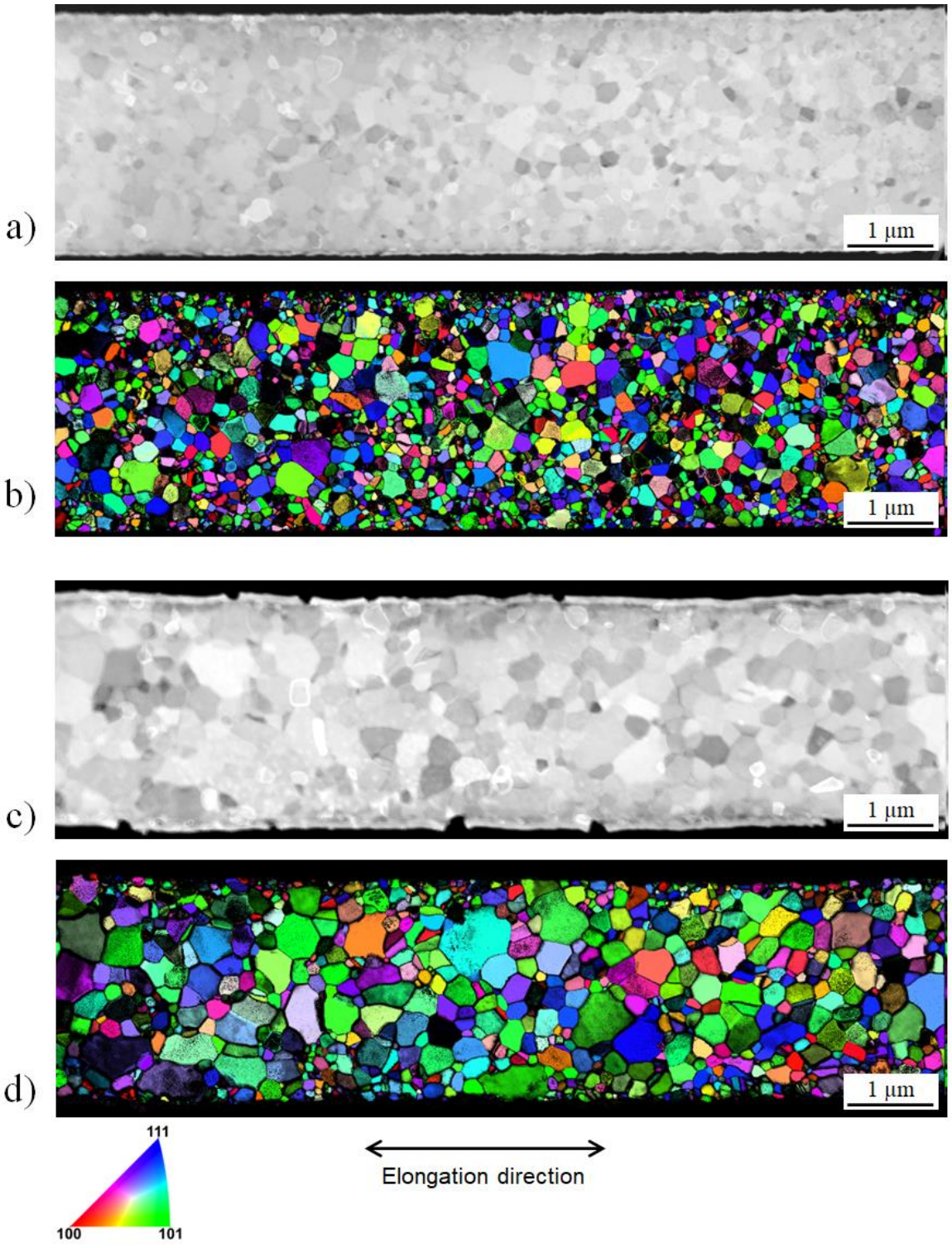

Figure 5 Microstructural characterization of an undeformed and a deformed specimen at 0.165: a) and c) show the virtual BF-STEM images of the undeformed and deformed specimen, respectively; b) and d) show the crystal orientation maps.

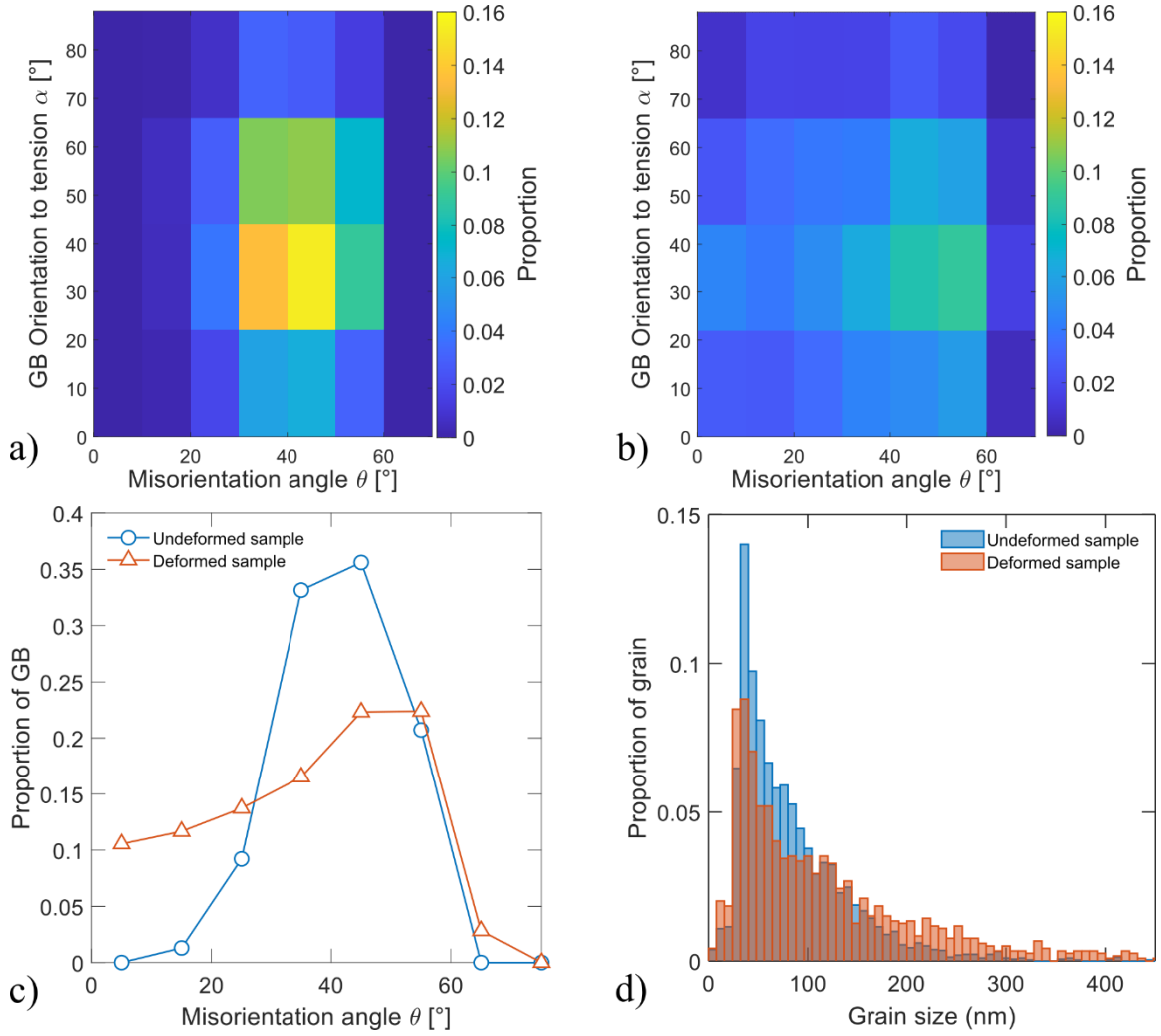

Figure 6 Proportion of GB as a function of misorientation angle and orientation to the tensile axis for a) the undeformed and b) the deformed specimen; c) distribution of misorientation angles for the undeformed and deformed specimen and d) grain size distribution for the undeformed and deformed specimen.

Fig. 7 compares the (111) and (110) pole figures of the undeformed (a) and deformed (b) specimens. The center of the pole figures corresponds to the film's normal direction (ND) whereas the tensile direction is horizontal. Both specimens exhibit a (111) fiber texture along ND. This results from crystal growth during film deposition. The experimental measurement does not show any significant evolution of the crystallographic texture during plastic deformation as confirmed when comparing Fig. 7.b to Fig. 7.c. The latter corresponds to the texture prediction of a crystal plasticity model which assumes {111}<110> dislocation slip (typical of coarse-grained Al) inside a uniformly deforming polycrystal (Taylor assumption). Dislocation-mediated plasticity would induce a progressive alignment of either a <111> direction, or a <100> direction, with the tensile axis. This does not occur in the TOC tensile tests. Instead, the random RBR of the pixel clusters (e.g. grains) determined by DIC (Fig. 4) are consistent with the resemblance of the two pole figures in Fig. 7.a-b. Indeed, according to DIC, grains tend to rotate around the film ND (e.g. around the center of the pole figure).

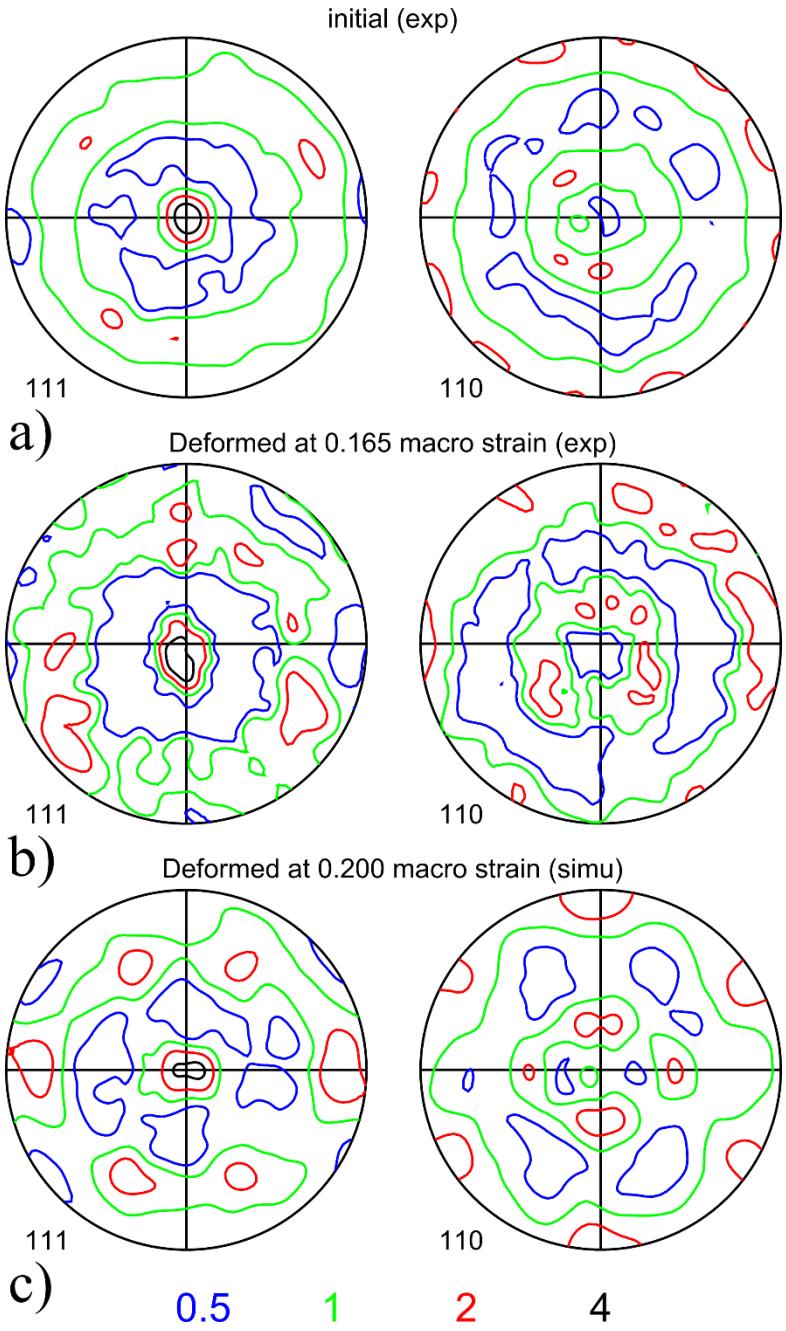

Figure 7 Pole figures obtained from: a) ACOM-TEM on the undeformed Al specimen; b) ACOM-TEM on the 0.165 deformed Al specimen (TOC 46) and c) result of a crystal plasticity simulation using as input the experimental initial texture, and assuming an elongation of 0.2 under uniaxial stress.

3.3. Correlative analysis by ACOM-TEM and nano-DIC

A combined analysis, involving nano-DIC followed by ACOM-TEM, is performed on the deformed TOC sample 46 (corresponding to an overall strain of 0.165). To allow the correlation of microstructure features, the microscopic deformation map obtained by DIC in the SEM (Fig. 8.a) and the crystal orientation map obtained by ACOM-TEM (Fig. 8.b-d) are resized and properly aligned, as detailed in the supplementary material (Fig. S10). The black lines appearing in Fig. 8.a correspond to the grain

boundaries identified by ACOM-TEM, which demonstrates that plastic yielding mainly localizes around the GB. Fig. 8.b-c-d show, respectively, the KAM map, the GB misorientation angles, and the GB geometrical resolved shear stress (GBRSS). The GBRSS is calculated as equal to $\cos(\alpha)\sin(\alpha)$, with α the angle between the GB plane normal and the tensile axis for a unitary stress amplitude (see Fig. 8.d). The latter is computed by accounting for the tilt angle of GB w.r.t. the tensile axis and by assuming that the GB planes are aligned parallel with the ND. This factor ranges from 0 for GB either perpendicular or parallel to the tensile axis to 0.5 for GB tilted at ±45°. This geometrical estimate of the local shear stress along the GB plane disregards the heterogeneity of the stress distribution across a plastically deforming polycrystal [26]. The hypothesis of predominantly in-plane deformation and rotation is supported by the sharp contrast of most GBs in the correlation coefficient map (supplementary material: Fig. S4.c), indicating that GBs are almost parallel to the film growth direction (maximum tilting of 14° to the ND). Such columnar grain shapes tend to impede out-of-plane rotation. Additionally, the geometrical constraint – far from being equiaxed – in the plane parallel to the film growth further limits the grains' out-of-plane sliding.

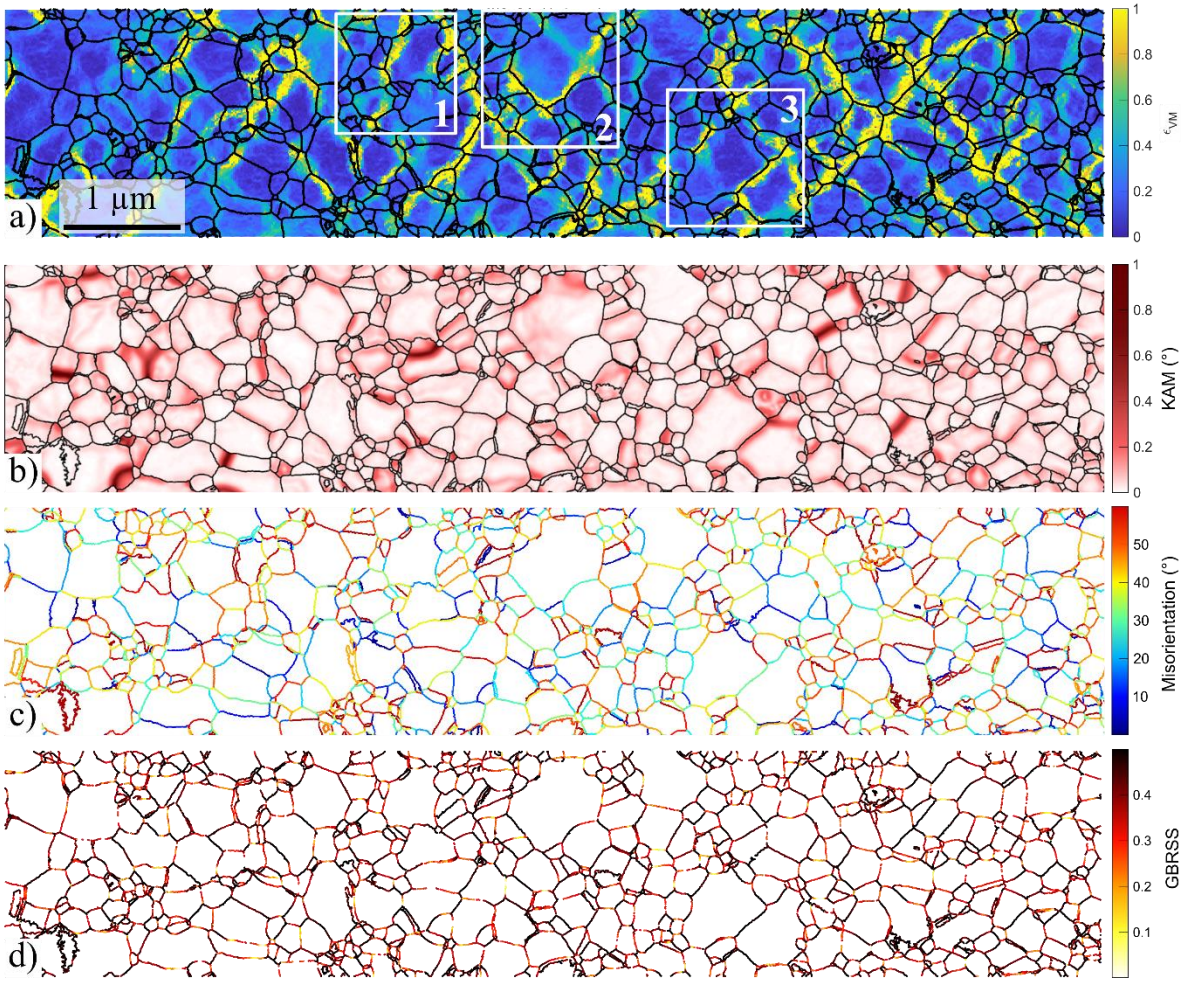

Figure 8 a) Comparison of nano-DIC equivalent Von Mises strain to TEM microstructure of the deformed specimen. Three zones are highlighted by white squares and detailed in Fig. 8; b) KAM map; c) GB misorientation and d) GB geometrical resolved shear stress.

The local comparison of the nano-DIC measurement (ϵ_{VM}) to the ACOM-TEM measurement (KAM) follows different trends in certain locations. This is for instance the case for Regions 1 and 2 highlighted in Fig. 8.a, for which a close-up is presented in Fig. 9. Region 3 is presented in supplementary material, Fig. S13.

Fig. 9.a and b show the KAM map, Fig. 9.c and 9.d show the equivalent von Mises strain maps and Fig. 9.e and 9.f show the bright field TEM image of zones 1 and 2, respectively. In the DIC maps presented in Fig. 9.c and 9.d, plastic deformation localizes mostly along GB associated with low KAM value. However, the dotted lines in Fig. 9.d highlight two intragranular shear bands which are aligned with the traces of the most active dislocation slip planes according to crystal plasticity calculations (Taylor model). Such intragranular deformation is seen neither in the KAM map (Fig. 9.b) nor in the bright field TEM image (Fig. 9.f). The contrast of the bright field image is known to vary as a function of the tilting of the specimen relative to the electron beam. The black arrows in Fig. 9.b-d-f point to an undeformed grain (according to nano-DIC) which hosts low KAM values. This undeformed grain surrounded by highly deformed regions, at the grain boundaries, thus undergoes a rigid body motion. On the other hand, the white arrow in Fig. 9.a-c-e shows that the high local KAM value does not scale with the local equivalent strain nor with the contrast of the bright field image.

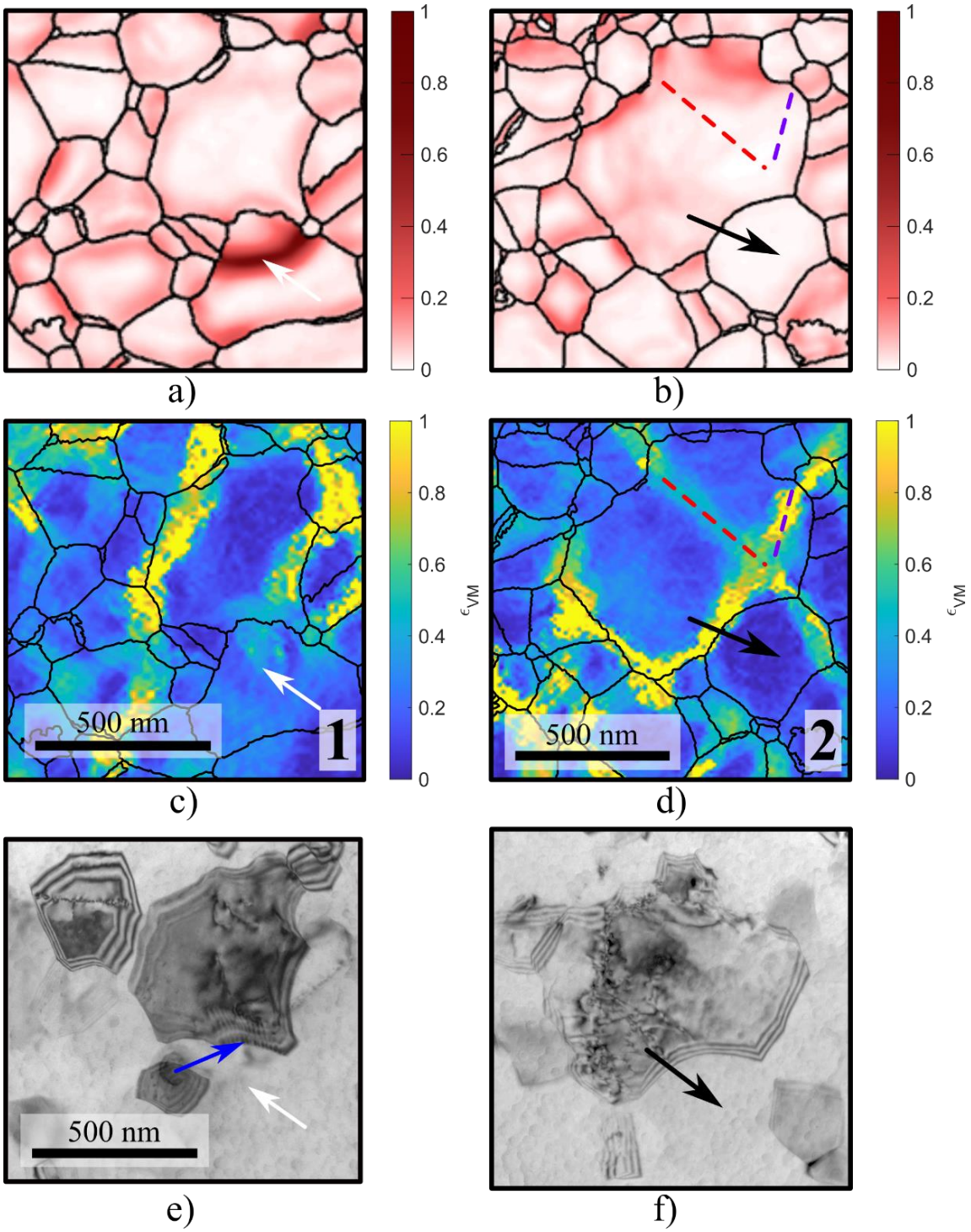

354

355 *Figure 9 Characterization of plastic localization and lattice distortions based on the combined use of a-b) KAM map from*
356 *ACOM-TEM, c-d) equivalent Von Mises strain map from nano-DIC and e-f) BFTEM images. Dotted lines show intragranular*
357 *shear bands parallel to two dislocation slip planes. Black and white arrows show regions of the maps where the three*
358 *experimental methods tend to either agree or disagree. The blue arrow shows line defects (disconnections) at GB.*

359 By combining nano-DIC and ACOM-TEM, it is possible to check whether the local strain amplitude is
360 correlated with the characteristics of GB segments. For that purpose, the GBRSS is discretized by steps
361 of 0.1 from 0 to 0.5 and the same is done for misorientation (measured after deformation) with

discretization steps of 10° from 0 to 70°. A matrix of 5×7 GBRSS and misorientation couples is created. Fig. 10.a shows the average deformation calculated inside a 10 pixel-thick layer along the GBs for the GBRSS and misorientation couples detailed above. As expected from the tilting of GB shear bands at + and – 45°, the local value of the equivalent von Mises strain scales with the GBRSS. However, the misorientation also seems to play a role: the local equivalent strain is low when the GB misorientation is less than 20°, and it is the highest for GB misorientations between 30° and 40°. The average strain associated with a type of GB is not fully representative of the local deformation since the strain distribution within GBs is not uniform. Fig. 10.b presents the cumulative distributions of equivalent strain in GBs with GBRSS between 0.4 and 0.5, as highlighted by the white dashed rectangle in Fig. 10.a. Three misorientation ranges are shown – i.e. (0-20°), (20-40°) and (40-60°). The GBs with 20-40 misorientation range show the highest equivalent strain compared to 0-20° and 40-60°. Also, the cumulative distribution of the GBs with 20° to 40° misorientation angles shows a sharp increase for equivalent von Mises strain higher than 0.9, confirming the large proportion of highly deformed GBs for this range of GB misorientations.

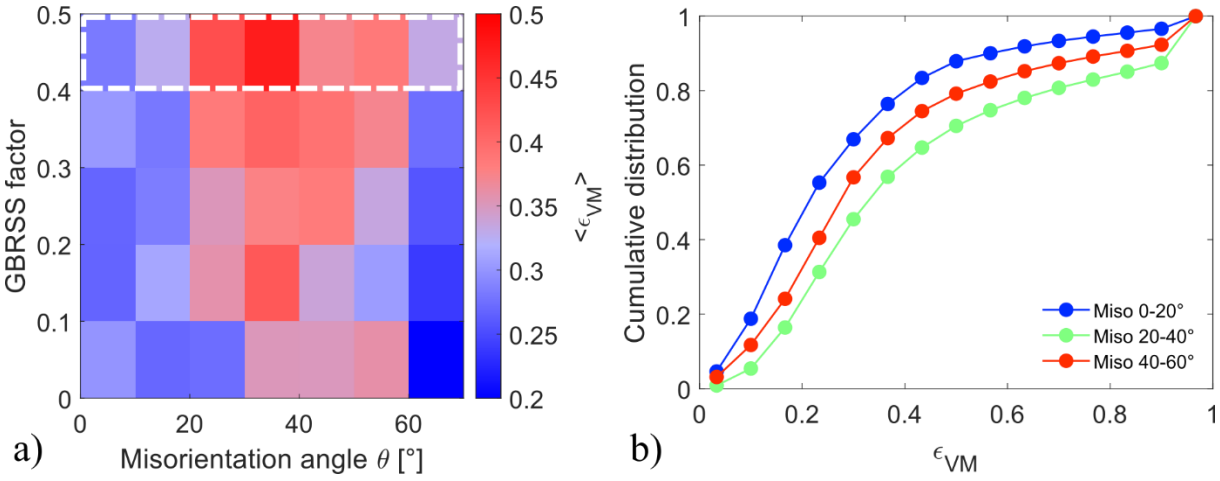

Figure 10 Local strain state associated with GB character characterized from ACOM-TEM: a) average equivalent von Mises strain as a function of GBRSS and misorientation (measured after deformation) and b) cumulative distribution of local von Mises strain for GBs with GBRSS between 0.4 and 0.5 and different GB misorientation ranges.

4. Discussion

The unique experimental investigation performed in this research offers new quantitative insight into the physical interplay between plastic deformation and the microstructure in nanocrystalline films. The complementarity of nano-DIC and ACOM-TEM enables the extraction of data both from the GB scale and from a more global statistical viewpoint. In the following, the macroscopic mechanical behavior is related to the total strain field and microstructure in order to isolate the dominant physical

scenarios responsible for the high ductility of these aluminum freestanding films. These films are indeed representative of a wider class of FCC nanostructured systems.

The large ductility of the Al films with overall total elongation above 15 % appears connected to a strong strain delocalization phenomenon. Strain delocalization – i.e. absence of catastrophic shear band or narrow neck development after the onset of the first necks – has been evidenced for a number of equivalent micro-scale specimens in the literature [10,11]. The main evidence of strain delocalization is the presence of multiple or diffuse necking zones along the sample gauge. In this study, most moderately deformed structures (macroscopic strain larger than 0.025) show early development of multiple necks, as highlighted by arrows in Fig. 2.b. The average strain along the gauge length of different specimens deformed between 0.025 and 0.152 is not constant (see Fig. 2.c). Moreover, the large strain regions expand as the macroscopic strain increases (see specimens strained at 0.052 and 0.073 in Fig. 2.c). Among measurements performed before failure (Fig. 2.c), the highest value of the section-averaged longitudinal strain is 0.42. Early necking initiation is presumably due to a limited initial strain hardening capacity at small plastic strains combined with significant geometrical imperfections [7]. The fact that plasticity does not localize further and that the early necks get stabilized can be related to the moderately high strain rate sensitivity ($m \approx 0.05$) and, maybe, to an increasing strain hardening capacity [7]. These findings will be further discussed in light of the strain field and microstructure evolution.

GB plastic activity is evidenced by complementary observations of the local strains measured by nano-DIC and the pole figures obtained by ACOM-TEM. Fig. 8.a demonstrates that most of the highly deformed regions coincide with GBs, suggesting that GB-driven plasticity mechanisms are dominant (see also Fig. S11 in supplementary material). Plastic localization bands are mostly tilted close to 45° with respect to the tensile loading direction implying that they host intense shear deformation along the direction of maximum resolved shear stress (see also Fig. 9.d). This evidences that GBs undergo cooperative sliding processes accommodating the RBR of the grains (Fig. 4). The comparison of the pole figures obtained experimentally and numerically (Fig. 7.b-c) also highlights that classical dislocation mediated plasticity is not the mechanism at play. This was also reported by Yang *et al.* for UFG Pd [29]. Finally, the strain field measurements on several specimens deformed between 0.023 and 0.059 (see Fig. 3) show localized curly structures, which look like grain boundaries. Even though the microstructure of the latter specimens was not characterized, it seems that GB plasticity is triggered at the early stage of the plastic deformation. Indeed, GB sliding has been shown to initiate under very low macro-strain to accommodate elastic anisotropy in millimeter-size samples [14,21,39]. GB sliding is known to be thermally activated [7,21,24], which supports the strain delocalization capacity described in the former paragraph.

Grain rotation is observed in the specimen TOC 46 and further highlighted in TOC 32 (see Fig. 4). Grain rotation was previously quantified for Al-based thin films – i.e. between 2 and 4° – using ASTAR TEM measurements and confirmed by MD simulations [14,55,67]. The present study shows that small clusters tend to undergo larger rotations than large clusters (Fig. 4.f).

The distribution of GB misorientations evolves during plastic deformation (see section 3.2). The tendency to evolve towards a low GB misorientation angle during deformation (see Fig. 6.c) has never been highlighted for such a large number of GBs, at this scale, to the best knowledge of the authors. The strain along the GB location depends on the GBRSS, which was reported previously [41,68], but it depends also on the GB misorientation angle (see Fig. 10). The relationship between the GB misorientation and GB sliding has been discussed by several authors and is still an open subject in the literature. Molecular dynamics simulations were performed on an Al bi-crystal, oriented with a [111] normal, to characterize the GB energy as a function of the misorientation [69,70]. These studies also link the GB energy to the propensity to deform by shear under stress. Considering experimental results in the literature, no direct correlation between the GB energy and GB sliding was shown. GB sliding is influenced by a number of other factors, such as GBRSS, GB grooves or disconnections [14,21,41,68]. Nevertheless, Linne *et al.* showed that even though the GB energy is not the main driving force for GB sliding in polycrystals, a synergy exists between the GB energy and increased GB sliding activity [41]. The latter observation is in line with our statistical study for which the highest GB energy – i.e. misorientation between 20 and 40 , estimated by MD bicrystals simulations [69,70] – corresponds to regions undergoing the largest plastic strain, especially for the high GBRSS values. Therefore, the evolution of GB character toward lower misorientation during deformation might be partly driven by the fact that GB misorientations between 20 and 40° correspond to high-energy GBs. These high-energy GBs can slide more easily and promote grain rotation, which finally leads to a decrease in the overall GB misorientation (Fig. 6c).

The latter scenario does not explain the significant grain growth mechanism shown in Fig. 5 and Fig. 6.d. When comparing the undeformed and deformed microstructures (see Fig. 5), the average grain size is significantly larger for the sample deformed at 0.165 (see Fig. 6.d). This phenomenon was evidenced by many authors, especially for nanocrystalline aluminum [14,21,43,44,56]. Grain rotation may promote grain growth by aligning neighboring crystals. However, it is often associated with softening and strain localization, which is the opposite of what is observed here [44,71]. Guo *et al.* assessed that both atomic shuffling, disconnections and Frank-Bilby dislocation activities are at work and favor GB migration in the case of mixed GBs [72]. Disconnections are line defects that are present

455 at GBs with a partial dislocation (or Burgers vector) and a partial step character [73]. These are, thus,
456 neither pure dislocations nor pure steps. The presence of disconnections at some GB observed by TEM
457 in our sample (blue arrow in Fig. 9e) is coherent with a grain growth mechanism. Indeed disconnections
458 induce shear-coupled GB migration and grain rotation by their cooperative motion [48,56]. This
459 represents an alternative mechanism of plastic deformation [23,48]. In the present work, shear-
460 coupled GB migration can also reduce the GB misorientation if the high-angle GBs (HAGBs) migrate
461 and leave behind low-angle GBs (LAGBs). One fundamental question emerges at this stage: why is
462 shear-coupled GB migration more effective for the 20°-40° GBs?
463
464 The presence of disconnections is confirmed using multiple micrographs under varying projections (see
465 Fig. 9a and supplementary material Fig. S12 and S13). However, the full characterization of these
466 defects in polycrystals is very challenging since it often requires very specific diffraction conditions that
467 are not always met. The small Burgers vector of some disconnections makes it even more difficult. This
468 explains why the study of these defects is often performed on bi-crystals or selected GBs in UFG thin
469 films in the literature [74–76]. Note also that, our *post-mortem* observations are made in a fully relaxed
470 film (after FIB cut). Thus, many disconnections could easily escape to the free surfaces of the thin film.
471 These difficulties did not allow concluding on the link between active 20°-40° GBs and disconnections.
472 Nevertheless, our results tend to indicate that GB sliding associated with both grain growth and grain
473 rotation promotes the transition from HAGBs to LAGBs, which should contribute to a decrease in the
474 energy of GBs and propensity to shear. This, finally, acts as a hardening mechanism by inhibiting GB
475 sliding processes. Moreover, by increasing the grain size distribution, grain rotation is further reduced
476 and intra-granular dislocation-based plasticity is triggered, which necessitates a larger critical stress
477 [21]. Intra-granular plasticity is observed in the nano-DIC strain map, in large grains (see Fig. 9.d). The
478 highlighted shear bands are perfectly correlated with crystal plasticity simulations, from which one can
479 obtain the most favorable slip system in the considered crystals, subjected to uniaxial tensile loading.
480 No correspondence of these lines was found in the KAM map (Fig. 9.b) and BFTEM micrographs
481 (Fig. 9.f), suggesting that a large number of glissile dislocations slipped along those lines and most of
482 them presumably disappeared by starvation or by some reverse motion due to back stress during
483 unloading [77]. Very few occurrences of shear bands were found in the specimen so it is not expected
484 that intra-granular plasticity triggers GB sliding mechanisms. Instead, intra-granular deformations
485 might develop in larger grains, when GBs cannot accommodate the strain [21].

5. Conclusion

High-resolution nano-DIC, on-chip testing and ACOM-TEM techniques were combined to unravel the plasticity mechanisms underlying the remarkable strain delocalization propensity of nanocrystalline Al films, at a scale never resolved before. The main findings of this research are:

- Multiple necks develop along the tensile specimens already after 0.025 macro-strain, but remaining essentially stable. The local strains within the final necking zone can reach values up to 0.45 before failure.
- Strong plastic delocalization is shown to be promoted by GB plasticity, including GB migration – i.e. grain growth – and grain rotation. These mechanisms are thermally activated, explaining the large strain rate sensitivity of the material [7,11,14].
- The distribution of misorientation angles between grains significantly changes during deformation, which is evidenced by an overall GB misorientation reduction. Also, maximum strain within GBs occurs for misorientation between 20° and 40° which are the GBs involving the highest energy, according to bicrystal MD simulations [69,70]. Even though it is not claimed that GB energy is the only significant parameter to trigger GBS, a strong correlation is found between the GB energy as studied in the literature and its propensity to slide [41]. Therefore, reducing GB misorientation during deformation might procure some slight strain hardening and contribute to mitigating catastrophic necking.
- Disconnections are observed at some GB and could explain the significant grain growth related to GB migration during deformation. In-situ TEM experiments are needed in order to further elucidate the possible link between disconnections and the more active GBs.

GB sliding, migration and grain rotation thus cooperate and compete, leading to a high ductility. The multiscale experiment approach adopted in the present work sheds new light on the role of general GBs in the mechanical response of UFG films dominated by GB-mediated plasticity.

Acknowledgements:

The authors would like to warmly thank the support of the teams of the UCLouvain WINFAB cleanroom and LACAMI platforms. This work was supported by the FNRS under Grant PDR T.0178.19 and by the FRFS-WEL-T WEL Research Institute under grant WEL-T-CR-2023 A – 06. H. Idrissi and L. Delannay are mandated by the Belgian National Fund for Scientific Research (FSR- FNRS).

References

[1] W. D. Nix, Elastic and plastic properties of thin films on substrates: nanoindentation techniques, Materials Science and Engineering: A 234–236 (1997) 37–44. https://doi.org/10.1016/S0921-5093(97)00176-7.

[2] R.A. Mesquita, C.A. Schuh, Tool steel coatings based on niobium carbide and carbonitride compounds, Surface and Coatings Technology 207 (2012) 472–479. https://doi.org/10.1016/j.surfcoat.2012.07.052.

[3] M. Li, H.X. Tang, M.L. Roukes, Ultra-sensitive NEMS-based cantilevers for sensing, scanned probe and very high-frequency applications, Nature Nanotechnology 2 (2007) 114–120. https://doi.org/10.1038/nnano.2006.208.

[4] N. André, M. Coulombier, V. De Longueville, D. Fabrègue, T. Gets, S. Gravier, T. Pardoen, J.-P. Raskin, Microfabrication-based nanomechanical laboratory for testing the ductility of submicron aluminium films, Microelectronic Engineering 84 (2007) 2714–2718. https://doi.org/10.1016/j.mee.2007.05.039.

[5] M. Dao, L. Lu, R. Asaro, J. Dehosson, E. Ma, Toward a quantitative understanding of mechanical behavior of nanocrystalline metals, Acta Materialia 55 (2007) 4041–4065. https://doi.org/10.1016/j.actamat.2007.01.038.

[6] Q. Han, X. Yi, A unified mechanistic model for Hall–Petch and inverse Hall–Petch relations of nanocrystalline metals based on intragranular dislocation storage, Journal of the Mechanics and Physics of Solids 154 (2021) 104530. https://doi.org/10.1016/j.jmps.2021.104530.

[7] T. Pardoen, Size and rate dependent necking in thin metallic films, Journal of the Mechanics and Physics of Solids 62 (2014) 81–98. https://doi.org/10.1016/j.jmps.2013.09.006.

[8] M. Dao, L. Lu, Y.F. Shen, S. Suresh, Strength, strain-rate sensitivity and ductility of copper with nanoscale twins, Acta Materialia 54 (2006) 5421–5432. https://doi.org/10.1016/j.actamat.2006.06.062.

[9] M.-S. Colla, B. Wang, H. Idrissi, D. Schryvers, J.-P. Raskin, T. Pardoen, High strength-ductility of thin nanocrystalline palladium films with nanoscale twins: On-chip testing and grain aggregate model, Acta Materialia 60 (2012) 1795–1806. https://doi.org/10.1016/j.actamat.2011.11.054.

[10] D.T. Read, Y.-W. Cheng, R.R. Keller, J.D. McColskey, Tensile properties of free-standing aluminum thin films, Scripta Materialia 45 (2001) 583–589. https://doi.org/10.1016/S1359-6462(01)01067-3.

[11] A. Pineau, A. Amine Benzerga, T. Pardoen, Failure of metals III: Fracture and fatigue of nanostructured metallic materials, Acta Materialia 107 (2016) 508–544. https://doi.org/10.1016/j.actamat.2015.07.049.

[12] A. Kobler, A. Kashiwar, H. Hahn, C. Kübel, Combination of in situ straining and ACOM TEM: A novel method for analysis of plastic deformation of nanocrystalline metals, Ultramicroscopy 128 (2013) 68–81. https://doi.org/10.1016/j.ultramic.2012.12.019.

[13] A. Kobler, J. Lohmiller, J. Schäfer, M. Kerber, A. Castrup, A. Kashiwar, P.A. Gruber, K. Albe, H. Hahn, C. Kübel, Deformation-induced grain growth and twinning in nanocrystalline palladium thin films, Beilstein J. Nanotechnol. 4 (2013) 554–566. https://doi.org/10.3762/bjnano.4.64.

[14] H. Idrissi, A. Kobler, B. Amin-Ahmadi, M. Coulombier, M. Galceran, J.-P. Raskin, S. Godet, C. Kübel, T. Pardoen, D. Schryvers, Plasticity mechanisms in ultrafine grained freestanding aluminum thin films revealed by *in-situ* transmission electron microscopy nanomechanical testing, Applied Physics Letters 104 (2014) 101903. https://doi.org/10.1063/1.4868124.

[15] J. Lohmiller, M. Grewer, C. Braun, A. Kobler, C. Kübel, K. Schüler, V. Honkimäki, H. Hahn, O. Kraft, R. Birringer, P.A. Gruber, Untangling dislocation and grain boundary mediated plasticity in nanocrystalline nickel, Acta Materialia 65 (2014) 295–307. https://doi.org/10.1016/j.actamat.2013.10.071.

[16] H. Idrissi, B. Wang, M.S. Colla, J.P. Raskin, D. Schryvers, T. Pardoen, Ultrahigh Strain Hardening in Thin Palladium Films with Nanoscale Twins, Advanced Materials 23 (2011) 2119–2122. https://doi.org/10.1002/adma.201004160.
[17] B. Wang, H. Idrissi, H. Shi, M.S. Colla, S. Michotte, J.P. Raskin, T. Pardoen, D. Schryvers, Texture-dependent twin formation in nanocrystalline thin Pd films, Scripta Materialia 66 (2012) 866–871. https://doi.org/10.1016/j.scriptamat.2012.01.038.
[18] M.-S. Colla, B. Amin-Ahmadi, H. Idrissi, L. Malet, S. Godet, J.-P. Raskin, D. Schryvers, T. Pardoen, Dislocation-mediated relaxation in nanograined columnar palladium films revealed by on-chip time-resolved HRTEM testing, Nat Commun 6 (2015) 5922. https://doi.org/10.1038/ncomms6922.
[19] A. Kashiwar, H. Hahn, C. Kübel, In Situ TEM Observation of Cooperative Grain Rotations and the Bauschinger Effect in Nanocrystalline Palladium, Nanomaterials 11 (2021) 432. https://doi.org/10.3390/nano11020432.
[20] F. Mompiou, D. Caillard, M. Legros, H. Mughrabi, In situ TEM observations of reverse dislocation motion upon unloading in tensile-deformed UFG aluminium, Acta Materialia 60 (2012) 3402–3414. https://doi.org/10.1016/j.actamat.2012.02.049.
[21] F. Mompiou, M. Legros, A. Boé, M. Coulombier, J.-P. Raskin, T. Pardoen, Inter- and intragranular plasticity mechanisms in ultrafine-grained Al thin films: An in situ TEM study, Acta Materialia 61 (2013) 205–216. https://doi.org/10.1016/j.actamat.2012.09.051.
[22] H. Rösner, C. Kübel, Y. Ivanisenko, L. Kurmanaeva, S.V. Divinski, M. Peterlechner, G. Wilde, Strain mapping of a triple junction in nanocrystalline Pd, Acta Materialia 59 (2011) 7380–7387. https://doi.org/10.1016/j.actamat.2011.08.020.
[23] J. Rajagopalan, J.H. Han, M.T.A. Saif, Plastic Deformation Recovery in Freestanding Nanocrystalline Aluminum and Gold Thin Films, Science 315 (2007) 1831–1834. https://doi.org/10.1126/science.1137580.
[24] J.P. Liebig, M. Mačković, E. Spiecker, M. Göken, B. Merle, Grain boundary mediated plasticity: A blessing for the ductility of metallic thin films?, Acta Materialia 215 (2021) 117079. https://doi.org/10.1016/j.actamat.2021.117079.
[25] V. Turlo, T.J. Rupert, Grain boundary complexions and the strength of nanocrystalline metals: Dislocation emission and propagation, Acta Materialia 151 (2018) 100–111. https://doi.org/10.1016/j.actamat.2018.03.055.
[26] W. Chrominski, M. Lewandowska, Mechanisms of plastic deformation in ultrafine-grained aluminium – In-situ and ex-post studies, Materials Science and Engineering: A 715 (2018) 320–331. https://doi.org/10.1016/j.msea.2017.12.083.
[27] J. Cappola, J. Wang, L. Li, A dislocation-density-based crystal plasticity model for FCC nanocrystalline metals incorporating thermally-activated depinning from grain boundaries, International Journal of Plasticity 172 (2024) 103863. https://doi.org/10.1016/j.ijplas.2023.103863.
[28] Yu. Ivanisenko, W. Skrotzki, R. Chulist, T. Lippmann, L. Kurmanaeva, Texture development in a nanocrystalline Pd–Au alloy studied by synchrotron radiation, Scripta Materialia 66 (2012) 131–134. https://doi.org/10.1016/j.scriptamat.2011.10.004.
[29] K. Yang, H. Fecht, Y. Ivanisenko, First Direct In Situ Observation of Grain Boundary Sliding in Ultrafine Grained Noble Metal, Adv Eng Mater 16 (2014) 517–521. https://doi.org/10.1002/adem.201300413.
[30] S.J. Sun, Y.Z. Tian, H.R. Lin, Z.J. Wang, Z.F. Zhang, Revisiting the role of prestrain history in the mechanical properties of ultrafine-grained CoCrFeMnNi high-entropy alloy, Materials Science and Engineering: A 801 (2021) 140398. https://doi.org/10.1016/j.msea.2020.140398.
[31] A. Kobler, C. Brandl, H. Hahn, C. Kübel, In situ observation of deformation processes in nanocrystalline face-centered cubic metals, Beilstein J. Nanotechnol. 7 (2016) 572–580. https://doi.org/10.3762/bjnano.7.50.

[32] J.P.M. Hoefnagels, M.P.F.H.L. van Maris, T. Vermeij, One-step deposition of nano-to-micron-scalable, high-quality digital image correlation patterns for high-strain *in-situ* multi-microscopy testing, Strain 55 (2019) e12330. https://doi.org/10.1111/str.12330.
[33] B. Winiarski, G.S. Schajer, P.J. Withers, Surface Decoration for Improving the Accuracy of Displacement Measurements by Digital Image Correlation in SEM, Exp Mech 52 (2012) 793–804. https://doi.org/10.1007/s11340-011-9568-y.
[34] N. Klavzer, S.F. Gayot, M. Coulombier, B. Nysten, T. Pardoen, Nanoscale digital image correlation at elementary fibre/matrix level in polymer–based composites, Composites Part A: Applied Science and Manufacturing 168 (2023) 107455. https://doi.org/10.1016/j.compositesa.2023.107455.
[35] S. Zhang, A. Godfrey, C. Zhang, W. Liu, D. Juul Jensen, Surface patterning for combined digital image correlation and electron backscatter diffraction in-situ deformation experiments, Materials Characterization 164 (2020) 110332. https://doi.org/10.1016/j.matchar.2020.110332.
[36] S. Yamasaki, H. Matsuo, T. Morikawa, M. Tanaka, Acquisition of microscopic and local stress-strain curves by combination of HR-EBSD and DIC methods, Scripta Materialia 235 (2023) 115603. https://doi.org/10.1016/j.scriptamat.2023.115603.
[37] T. Vermeij, J.P.M. Hoefnagels, Plasticity, localization, and damage in ferritic-pearlitic steel studied by nanoscale digital image correlation, Scripta Materialia 208 (2022) 114327. https://doi.org/10.1016/j.scriptamat.2021.114327.
[38] M.A. Linne, A. Venkataraman, M.D. Sangid, S. Daly, Grain Boundary Sliding and Slip Transmission in High Purity Aluminum, Exp Mech 59 (2019) 643–658. https://doi.org/10.1007/s11340-019-00517-z.
[39] A. Venkataraman, M. Linne, S. Daly, M.D. Sangid, Criteria for the prevalence of grain boundary sliding as a deformation mechanism, Materialia 8 (2019) 100499. https://doi.org/10.1016/j.mtla.2019.100499.
[40] T. Vermeij, C.J.A. Mornout, V. Rezazadeh, J.P.M. Hoefnagels, Martensite plasticity and damage competition in dual-phase steel: A micromechanical experimental–numerical study, Acta Materialia 254 (2023) 119020. https://doi.org/10.1016/j.actamat.2023.119020.
[41] M.A. Linne, T.R. Bieler, S. Daly, The effect of microstructure on the relationship between grain boundary sliding and slip transmission in high purity aluminum, International Journal of Plasticity 135 (2020) 102818. https://doi.org/10.1016/j.ijplas.2020.102818.
[42] B. Yavuzyegit, E. Avcu, A.D. Smith, J.M. Donoghue, D. Lunt, J.D. Robson, T.L. Burnett, J.Q. da Fonseca, P.J. Withers, Mapping plastic deformation mechanisms in AZ31 magnesium alloy at the nanoscale, Acta Materialia 250 (2023) 118876. https://doi.org/10.1016/j.actamat.2023.118876.
[43] F. Mompiou, D. Caillard, M. Legros, Grain boundary shear–migration coupling—I. In situ TEM straining experiments in Al polycrystals, Acta Materialia 57 (2009) 2198–2209. https://doi.org/10.1016/j.actamat.2009.01.014.
[44] M. Legros, D.S. Gianola, K.J. Hemker, In situ TEM observations of fast grain-boundary motion in stressed nanocrystalline aluminum films, Acta Materialia 56 (2008) 3380–3393. https://doi.org/10.1016/j.actamat.2008.03.032.
[45] Z. Shan, E.A. Stach, J.M.K. Wiezorek, J.A. Knapp, D.M. Follstaedt, S.X. Mao, Grain Boundary-Mediated Plasticity in Nanocrystalline Nickel, Science 305 (2004) 654–657. https://doi.org/10.1126/science.1098741.
[46] L. Wang, J. Teng, P. Liu, A. Hirata, E. Ma, Z. Zhang, M. Chen, X. Han, Grain rotation mediated by grain boundary dislocations in nanocrystalline platinum, Nat Commun 5 (2014) 4402. https://doi.org/10.1038/ncomms5402.
[47] Q. Li, L. Wang, J. Teng, X. Pang, X. Han, J. Zou, In-situ observation of cooperative grain boundary sliding and migration in the nano-twinned nanocrystalline-Au thin-films, Scripta Materialia 180 (2020) 97–102. https://doi.org/10.1016/j.scriptamat.2020.01.025.
[48] A. Rajabzadeh, F. Mompiou, S. Lartigue-Korinek, N. Combe, M. Legros, D.A. Molodov, The role of disconnections in deformation-coupled grain boundary migration, Acta Materialia 77 (2014) 223–235. https://doi.org/10.1016/j.actamat.2014.05.062.

[49] F. Mompiou, M. Legros, Quantitative grain growth and rotation probed by in-situ TEM straining and orientation mapping in small grained Al thin films, Scripta Materialia 99 (2015) 5–8. https://doi.org/10.1016/j.scriptamat.2014.11.004.
[50] M.J. Hÿtch, A.M. Minor, Observing and measuring strain in nanostructures and devices with transmission electron microscopy, MRS Bull. 39 (2014) 138–146. https://doi.org/10.1557/mrs.2014.4.
[51] P.F. Rottmann, K.J. Hemker, Nanoscale elastic strain mapping of polycrystalline materials, Materials Research Letters 6 (2018) 249–254. https://doi.org/10.1080/21663831.2018.1436609.
[52] A. Després, M. Veron, Elastic strain field measurements in the TEM for metallurgical applications, Materials Characterization 202 (2023) 113012. https://doi.org/10.1016/j.matchar.2023.113012.
[53] D.S. Gianola, B.G. Mendis, X.M. Cheng, K.J. Hemker, Grain-size stabilization by impurities and effect on stress-coupled grain growth in nanocrystalline Al thin films, Materials Science and Engineering: A 483–484 (2008) 637–640. https://doi.org/10.1016/j.msea.2006.12.155.
[54] D. Fabrègue, N. André, M. Coulombier, J.P. Raskin, T. Pardoen, Multipurpose nanomechanical testing machines revealing the size-dependent strength and high ductility of pure aluminium submicron films, Micro Nano Lett. 2 (2007) 13. https://doi.org/10.1049/mnl:20065068.
[55] L. Bajtošová, B. Křivská, R. Králík, J. Veselý, J. Hanuš, P. Harcuba, J. Fikar, A. Yadav, M. Cieslar, Deformation mechanisms of Al thin films: In-situ TEM and molecular dynamics study, Scripta Materialia 215 (2022) 114688. https://doi.org/10.1016/j.scriptamat.2022.114688.
[56] T.J. Rupert, D.S. Gianola, Y. Gan, K.J. Hemker, Experimental Observations of Stress-Driven Grain Boundary Migration, Science 326 (2009) 1686–1690. https://doi.org/10.1126/science.1178226.
[57] S. Gravier, M. Coulombier, A. Safi, N. Andre, A. Boe, J.-P. Raskin, T. Pardoen, New On-Chip Nanomechanical Testing Laboratory - Applications to Aluminum and Polysilicon Thin Films, J. Microelectromech. Syst. 18 (2009) 555–569. https://doi.org/10.1109/JMEMS.2009.2020380.
[58] T. Pardoen, M.-S. Colla, H. Idrissi, B. Amin-Ahmadi, B. Wang, D. Schryvers, U.K. Bhaskar, J.-P. Raskin, A versatile lab-on-chip test platform to characterize elementary deformation mechanisms and electromechanical couplings in nanoscopic objects, Comptes Rendus Physique 17 (2016) 485–495. https://doi.org/10.1016/j.crhy.2015.11.005.
[59] M. Pletea, R. Koch, H. Wendrock, R. Kaltofen, O.G. Schmidt, *In situ* stress evolution during and after sputter deposition of Al thin films, J. Phys.: Condens. Matter 21 (2009) 225008. https://doi.org/10.1088/0953-8984/21/22/225008.
[60] T. Vermeij, J.A.C. Verstijnen, T.J.J. Ramirez y Cantador, B. Blaysat, J. Neggers, J.P.M. Hoefnagels, A Nanomechanical Testing Framework Yielding Front&Rear-Sided, High-Resolution, Microstructure-Correlated SEM-DIC Strain Fields, Exp Mech 62 (2022) 1625–1646. https://doi.org/10.1007/s11340-022-00884-0.
[61] J. Blaber, B. Adair, A. Antoniou, Ncorr: Open-Source 2D Digital Image Correlation Matlab Software, Exp Mech 55 (2015) 1105–1122. https://doi.org/10.1007/s11340-015-0009-1.
[62] M. Coulombier, P. Baral, A. Orekhov, R. Dohmen, J.P. Raskin, T. Pardoen, P. Cordier, H. Idrissi, On-chip very low strain rate rheology of amorphous olivine films, Acta Materialia (2024) 119693. https://doi.org/10.1016/j.actamat.2024.119693.
[63] M. Coulombier, G. Guisbiers, M.-S. Colla, R. Vayrette, J.-P. Raskin, T. Pardoen, On-chip stress relaxation testing method for freestanding thin film materials, Review of Scientific Instruments 83 (2012) 105004. https://doi.org/10.1063/1.4758288.
[64] D.S. Gianola, D.H. Warner, J.F. Molinari, K.J. Hemker, Increased strain rate sensitivity due to stress-coupled grain growth in nanocrystalline Al, Scripta Materialia 55 (2006) 649–652. https://doi.org/10.1016/j.scriptamat.2006.06.002.
[65] D. Caillard, J.L. Martin, Microstructure of aluminium during creep at intermediate temperature—I. dislocation networks after creep, Acta Metallurgica 30 (1982) 437–445. https://doi.org/10.1016/0001-6160(82)90224-3.
[66] C. Steger, An unbiased detector of curvilinear structures, IEEE Trans. Pattern Anal. Machine Intell. 20 (1998) 113–125. https://doi.org/10.1109/34.659930.

[67] S. Hocker, M. Hummel, P. Binkele, H. Lipp, S. Schmauder, Molecular dynamics simulations of tensile tests of Ni-, Cu-, Mg- and Ti-alloyed aluminium nanopolycrystals, Computational Materials Science 116 (2016) 32–43. https://doi.org/10.1016/j.commatsci.2015.07.047.
[68] I.A. Ovid'ko, A.G. Sheinerman, Enhanced ductility of nanomaterials through optimization of grain boundary sliding and diffusion processes, Acta Materialia 57 (2009) 2217–2228. https://doi.org/10.1016/j.actamat.2009.01.030.
[69] Y. Qi, P. Krajewski, Molecular dynamics simulations of grain boundary sliding: The effect of stress and boundary misorientation, Acta Materialia 55 (2007) 1555–1563. https://doi.org/10.1016/j.actamat.2006.10.016.
[70] P.R.M. van Beers, V.G. Kouznetsova, M.G.D. Geers, M.A. Tschopp, D.L. McDowell, A multiscale model of grain boundary structure and energy: From atomistics to a continuum description, Acta Materialia 82 (2015) 513–529. https://doi.org/10.1016/j.actamat.2014.08.045.
[71] M.A. Meyers, A. Mishra, D.J. Benson, Mechanical properties of nanocrystalline materials, Progress in Materials Science 51 (2006) 427–556. https://doi.org/10.1016/j.pmatsci.2005.08.003.
[72] Y. Guo, J. Teng, G. Yang, A. Li, Y. Deng, C. Yang, L. Wang, X. Yan, Z. Zhang, X. Li, E. Ma, X. Han, In situ observation of atomic-scale processes accomplishing grain rotation at mixed grain boundaries, Acta Materialia 241 (2022) 118386. https://doi.org/10.1016/j.actamat.2022.118386.
[73] J.P. Hirth, Dislocations, steps and disconnections at interfaces, Journal of Physics and Chemistry of Solids 55 (1994) 985–989. https://doi.org/10.1016/0022-3697(94)90118-X.
[74] V. Samaee, M. Dupraz, T. Pardoen, H. Van Swygenhoven, D. Schryvers, H. Idrissi, Deciphering the interactions between single arm dislocation sources and coherent twin boundary in nickel bi-crystal, Nat Commun 12 (2021) 962. https://doi.org/10.1038/s41467-021-21296-z.
[75] H. Idrissi, K. Renard, D. Schryvers, P.J. Jacques, TEM investigation of the formation mechanism of deformation twins in Fe–Mn–Si–Al TWIP steels, Philosophical Magazine 93 (2013) 4378–4391. https://doi.org/10.1080/14786435.2013.832837.
[76] L. Ding, A. Hilhorst, H. Idrissi, P.J. Jacques, Potential TRIP/TWIP coupled effects in equiatomic CrCoNi medium-entropy alloy, Acta Materialia 234 (2022) 118049. https://doi.org/10.1016/j.actamat.2022.118049.
[77] V. Samaee, R. Gatti, B. Devincre, T. Pardoen, D. Schryvers, H. Idrissi, Dislocation driven nanosample plasticity: new insights from quantitative in-situ TEM tensile testing, Sci Rep 8 (2018) 12012. https://doi.org/10.1038/s41598-018-30639-8.